# Contribution to the Understanding of Tribological Properties of Graphite Intercalation Compounds with Metal Chloride

**K. Delbé · J.-L. Mansot · Ph. Thomas · Ph. Baranek · F. Boucher · R. Vangelisti · D. Billaud**

**Abstract** Intrinsic tribological properties of lamellar compounds are usually attributed to the presence of van der Waals gaps in their structure through which interlayer interactions are weak. The controlled variation of the distances and interactions between graphene layers by intercalation of electrophilic species in graphite is used in order to explore more deeply the friction reduction properties of low-dimensional compounds. Three graphite intercalation compounds with antimony pentachloride, iron trichloride and aluminium trichloride are studied. Their tribological properties are correlated to their structural parameters, and the interlayer interactions are deduced from ab initio bands structure calculations.

**Keywords** Tribology · Bands structure calculations · Friction coefficient · Graphite intercalation compounds · Solid lubricant · Raman spectroscopy

K. Delbé
Laboratoire Génie de Production, EA 1905, École Nationale d'Ingénieurs de Tarbes, BP 1629, 65016 Tarbes Cedex, France

J.-L. Mansot (✉) · Ph. Thomas (✉)
Groupe de Technologie des Surfaces et Interfaces, EA 2432, Faculté des Sciences Exactes et Naturelles, Université des Antilles et de la Guyane, BP 250, 97157 Pointe-à-Pitre Cedex, Guadeloupe, France
e-mail: jean-louis.mansot@univ-ag.fr

Ph. Thomas
e-mail: philippe.thomas@univ-ag.fr

J.-L. Mansot
Centre Commun de Caractérisation des Matériaux des Antilles et de la Guyane (FED C3MAG), Faculté des Sciences Exactes et Naturelles, Université des Antilles et de la Guyane, BP 250, 97157 Pointe-à-Pitre Cedex, Guadeloupe, France

Ph. Baranek
EDF – R&D, Department MMC and MAI, Avenue des Renardières, Les Renardières, 77818 Moret sur Loing Cedex, France

F. Boucher
Laboratoire de Chimie des Solides, Institut des Matériaux Jean Rouxel, UMR 6502 CNRS-Université de Nantes, 2 rue de la Houssinière, BP 32229, 44322 Nantes Cedex 3, France

R. Vangelisti · D. Billaud
Institut Jean Lamour UMR 7198, équipe 205 matériaux carbonés, BP 239, 54506 Vandœuvre-lès-Nancy Cedex, France

## 1 Introduction

The good tribologic properties of lamellar compounds ($MoS_2$, graphite, etc.) are classically associated to their anisotropic structures [1–8] in which the intra layer covalent binding forces are much larger than the interlayer ones (van der Waals forces or weak orbital overlaps). These weak interlayer interactions are supposed to generate low-critical shear rate along directions parallel to the layers, resulting in a low-friction coefficient.

Considering this hypothesis, it should be theoretically possible to modulate the tribologic behaviour of lamellar compounds by modifying the nature and intensity of the interlayer interactions. Such modifications can be obtained by intercalation of chemical species in the van der Waals gaps of the lamellar materials. The synthesis of intercalation compounds with various chemical species at different concentrations was recognized of great interest in order to monitor the physical properties of the host materials such as electrical, thermal or magnetic properties [9–17]. In the case of graphite, the intercalation processes have been the object of numerous investigations since the 1930s [18, 19] as far as a large variety of reagents can be intercalated into

graphite according to its electronic structure: the graphene sheets can accommodate electron donor as well as electron acceptor species [20]. The intercalation processes are generally accompanied by oxido-reduction reactions implying the intercalated species and the host structure. These characteristics of the intercalation mechanism are at the origin of energy storage applications in the case of electron donor intercalants, typically alkali metals and more specifically lithium, to constitute electrode materials for batteries [21–26]. For electron acceptor intercalants, anionic species are intercalated into the oxidized graphite network [27–29]. In both cases, the obtained graphite intercalation compounds (GICs), present a lamellar structure in which the planar shape of the graphene layers remains unchanged. As first effects, the intercalation process leads to an enhancement of the interlayer distances and a modification of interlayer interactions subjected to influence the tribologic behaviour of the host structure.

The great interest generated by metal chloride–GICs is due to the enhancement of the in-layer conductivity by the intercalation process resulting from the charge transfer from the host structure to the electrophilic intercalant [27]. In spite of many X-ray diffraction, Mössbauer spectroscopy and electron microscopy experiments, the structures of these compounds are not completely established. The nature of the intercalated species and the stacking sequences along $\vec{c}$ axis are generally well identified, but the spatial distribution of the intercalated molecules in the van der Waals gaps are still not clearly determined [30–34]. The large $\vec{c}$ axis expansion resulting from the intercalation process is supposed to strongly modify the tribologic behaviour.

In this study, the tribologic properties of GICs prepared from selected transition metal chlorides species ($FeCl_3$, $SbCl_5$ and $AlCl_3$) are evaluated and compared to pristine graphite one.

Assuming a great similarity between the electronic structures of the GIC compounds, electronic structures of graphite and of the $AlCl_3$–GIC are established in order to evaluate the interlayer interactions and correlate their evolution to obtained friction properties.

## 2 Methodological Aspects

### 2.1 Experimental Approach

#### *2.1.1 Materials*

Three GICs are studied in this work. They result from the intercalation of iron (III) chloride ($FeCl_3$), aluminium (III) chloride ($AlCl_3$) and antimony (V) pentachloride ($SbCl_5$).

$FeCl_3$ and $AlCl_3$–GICs are prepared in the vapour phase by the standard two-temperature zone method in which the metal halide vapour reacts with graphite [35–37]. Commercial powder of $FeCl_3$ or $AlCl_3$ (Fluka, 99.9 %) and natural graphite from Madagascar are placed in the two compartments of a two-bulb Pyrex tube. The tube is then heated in a furnace in order to obtain two controlled temperature zones. The intercalation of $FeCl_3$ or $AlCl_3$ molecules (resulting from sublimation of the initial powder) is performed under chlorine atmosphere. Graphite is maintained at a temperature $T_G$ higher than the metal halide sublimation temperature in order to avoid the condensation of $MCl_x$ on the graphite surface. The experimental conditions are reported in Table 1.

**Table 1** Experimental conditions for the synthesis of $MCl_x$–GICs

| Intercalant | $T_M$ | $T_G$ | Duration | Composition |
|---|---|---|---|---|
| $FeCl_3$ | 300 °C | 320 °C | 2–5 days | $FeCl_3C_{5-9}$ [20] |
| $AlCl_3$ | 150 °C | 170 °C | 3 days | $AlCl_{3.3}C_{9-10}$ [21] |
| $SbCl_5$ | 165 °C | 170 °C | 12 h | $SbCl_5C_{12}$ [22] |

In the case of $SbCl_5$, the intercalation compound is obtained by direct action of liquid $SbCl_5$ (Sigma-Aldrich, 99.9 %) on pyrographite (PGCCL, Le Carbone Lorraine). In such conditions, $SbCl_5$ intercalates spontaneously into the graphitic structure to obtain the $SbCl_5C_{12}$ stoechiometry [25].

#### *2.1.2 Tribologic Tests*

The tribologic properties of the compounds are evaluated using an alternative ball-on-plane tribometer consisting of an AISI 52100 steel ball rubbing against an AISI 52100 steel plane (Table 2) on which the tested material is deposited.

**Table 2** Experimental parameters of the tribologic tests

| | |
|---|---|
| Steel ball | Metallurgy: AISI 52100 |
| | HV = 850 |
| | Young modulus: $E = 200$ GPa |
| | Diameter: 9.5 mm |
| | Roughness: $R_a = 90 \pm 10$ nm; $S_a = 120$ nm |
| Steel plane | Metallurgy AISI 52100 |
| | HV = 850 |
| | Young modulus: $E = 200$ GPa |
| | Roughness: $R_a = 350 \pm 10$ nm; $S_a = 405$ nm |
| Normal load | 10 N |
| Contact diameter (Hertz's theory) | 140 μm |
| Mean contact pressure | 0.65 GPa |
| Sliding speed | 6 mm $s^{-1}$ |

A normal load of 10 N is applied leading to a contact diameter of 140 μm (according to Hertz's theory) and a mean contact pressure of 0.65 Gpa. The sliding speed is 6 mm $s^{-1}$. The friction coefficient is measured with a computer-based data acquisition system.

Balls are used as delivered. Planes are polished to generate the desired roughness needed to improve the adherence of the tested solid films on the substrate surfaces. Surface roughness characterizations are performed by means of an optical Altisurf 500 profilometer allowing us to evaluate the 2D ($R_a$) and 3D ($S_a$) roughness parameters of the balls and the planes reported in Table 2.

Balls and planes are ultrasonically cleaned in ethanol and acetone in order to eliminate contaminants. The solid lubricant is deposited onto the plane by rubbing the tested GIC on the flat steel surface. Due to the sensitivity of the intercalation compounds to oxygen and moisture, the tribologic experiments are performed in a glove box under high-purity argon atmosphere ($[H_2O] < 20$ ppm, $[O_2] < 1$ ppm).

The friction coefficient measured during the first few cycles is considered to characterize the intrinsic tribologic properties of the materials. The evolution of the friction coefficient as a function of the cycle number is followed in order to investigate the friction properties changes induced by structural transformations of the initial materials during the friction process. Additional experiments are carried out by adding one drop of petroleum ether (PE) in order to facilitate the tribofilm formation as already shown in previous works [38, 39]. The friction coefficients of the "dry compounds" are measured after PE evaporation.

#### *2.1.3 Raman Investigations*

Raman spectroscopy studies of the initial compounds and of the tribofilms are performed with a HR 800 Horiba multi channel spectrometer using a Peltier cooled CCD detector for signal recording. The exciting line is 532 nm wavelength line (Nd YAG laser). The pre-monochromator is a notch filter and the monochromator a 300-lines/mm holographic grating. In our conditions (objective lens ×50, confocal hole 500 μm, spectrometer entry aperture 500 μm), the probe diameter is of 7 μm, the wavenumber resolution is of 10 $cm^{-1}$ and dispersion is 0.8 $cm^{-1}$/pixel. The laser power at the sample level is 30 mW, and acquisition time is in the range of 10–60 s depending on the sample thickness. Special attention is paid to avoid sample irradiation damages during the analyses.

### 2.2 Theoretical Approach

Ab initio calculations, in order to obtain bands structures and density of states (DOS) diagrams, were initiated using the Full-Linearized Augmented Plane Waves (FLAPW) method implemented in Wien2k code [40]. These calculations were then confirmed and completed (geometric optimization, van der Waals corrections and interlayer interactions) using the ab initio periodic CRYSTAL [41, 42] and VASP [43–45] codes. CRYSTAL permits to solve self-consistently both the Hartree–Fock (HF) and Kohn–Sham (KS) equations, as well as hybrid HF/KS schemes, using pseudopotential or all-electron Gaussian-type function (GTF) basis set through the standard linear combination of atomic orbital (LCAO) approach. The VASP code, on the other hand, uses density functional techniques, as well as hybrid schemes [46–49], with the plane wave ultrasoft pseudopotential of Vanderbilt (USPP) [48] or projected augmented plane wave (PAW) approaches [49, 50].

In this study, the exchange–correlation functional of Perdew et al. [51] based on the generalized gradient approximation (GGA) has been used.

Regarding the basis sets available in the library of the VASP code, we have employed the USPP pseudopotentials. In the present pseudopotentials, the aluminium and chlorine 3*s* and 3*p* and carbon 2*s* and 2*p* electrons were treated as valence electrons.

With CRYSTAL, the Al and C atoms have been described by an all-electron GTF basis set. Standard basis with 8511-1d* and 621-1d* has been adopted for Al and C, respectively. For Cl, the 3*s* and 3*p* have been treated as valence electrons combined with a Hay–Wadt small-core pseudopotential and a 31-1d* basis set.

With CRYSTAL, the 7 7 7 7 14 thresholds have been used for the Coulomb and exchange series. For VASP, we used a plane wave cut-off of 520 eV. For both codes, the calculations have been performed with an 10 × 10 × 10 Monkhorst–Pack *k*-point mesh [52]. The total energies and eigenvalues obtained with this mesh are determined with a precision of $10^{-4}$ eV, and the bond lengths are predicted with an error of less than 0.01 Å.

One of the delicate aspects in the evaluation of the energies of interaction (IE) between layers is that these last ones are very weak. The use of CRYSTAL allows us to obtain reliable and accurate primitive cell energy values in bulk 3D material and in isolated bi-dimensional layers (see calculation principle in Fig. 1).

The interaction energy between layers is obtained via the following formula:

$$\mathrm{IE} = E_{\mathrm{Bulk}} - E_{\mathrm{Isolated\ layer}}$$

where $E_{\mathrm{Bulk}}$ is the total energy of the primitive cell in the bulk material and $E_{\mathrm{Isolated\ layer}}$ is the total energy of the primitive cell in the isolated layer.

In order to take into account more reliably the contribution of the van der Waals interactions in the interlayer interaction energy calculations, the semi-empirical London dispersion type's correction, as proposed by Grimme [53,

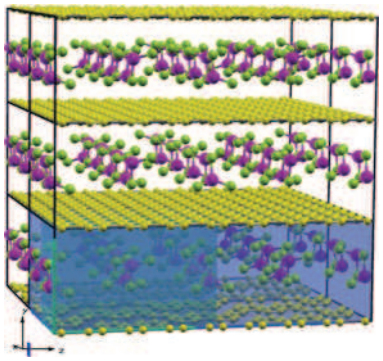

*Bulk (3D periodic system) with $E_{Bulk}$ as the total energy of the primitive cell material*

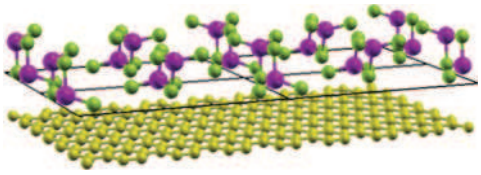

*Isolated layer (2D periodic system deduced from the bulk) with $E_{Isolated\ layer}$ as the total energy of the primitive cell of the isolated layer.*

$$IE = E_{Bulk} - E_{Isolated\ layer}$$

**Fig. 1** Method principle used for the determination of the interlayer energy of interaction (IE) for $Al_4Cl_{12}C_{48}$

54] (the D2-correction) implemented in CRYSTAL and VASP, was used. In this article, only the results obtained with CRYSTAL are reported (our available version of VASP do not possess this correction). But, as it is shown in Table 3 and in previous works [55, 56], both codes provide the same results on the structural and electronic properties of solids. The Grimme correction does not introduce heavy modifications in the calculated $a$ and $b$ lattice parameters (less than 0.05 %) as already noticed in previous works related to other molecular and layered materials [57–59]. This correction is used to obtain a best estimate of the interlayer interactions [57–59].

Graphite interlayer interaction in $AlCl_3$–GIC in eV/at

$IE_G = -0.045$ eV/at $IE_{GIC} = -0.001$ eV/at

## 3 Results

### 3.1 Structure of the Initial GICs

The studied materials are Stage 1 GICs. In such compounds, the intercalated molecules occupy all the van der Waals gaps. According to previous works [35, 36, 60], the interlayer distance, equal to 3.35 Å for pristine graphite, is strongly enhanced and raises 9.37, 9.44 and 9.56 Å for $FeCl_3$–GIC, $SbCl_5$–GIC and $AlCl_3$–GIC, respectively (Fig. 2). The lamellar structure of $MCl_x$–GICs is characterized by the graphene–chlorine–metal–chorine–graphene stacking sequence along $\vec{c}$ axis (Fig. 2). However, the exact position of the intercalant in the van der Waals gaps is still not exactly determined. As a consequence, geometric optimization procedure is used in order to determine the more probable position of the intercalated species in the

**Table 3** Theoretical determined geometries of $Al_4Cl_{12}C_{48}$

| Crystal's axes | $\vec{a}$ | | $\vec{b}$ | | $\vec{c}$ | |
|---|---|---|---|---|---|---|
| | VASP | CRYSTAL | VASP | CRYSTAL | VASP | CRYSTAL |
| Lattice parameters | 17.40 | 17.114 (17.112) | 7.41 | 7.414 (7.413) | 9.56 | |
| Atomic positions | | | | | | |
| Al | 0. | 0. | 0.3110 | 0.3143 (0.3147) | 0.4237 | 0.4177 (0.4168) |
| Cl1 | 0.8944 | 0.8936 (0.8936) | 0.1915 | 0.1946 (0.1951) | 0.3777 | 0.3659 (0.3644) |
| Cl2 | 0. | 0. | 0.6017 | 0.6095 (0.6105) | 0.3488 | 0.3512 (0.3516) |
| C1 | 0.7916 | 0.7917 (0.917) | 0. | 0. | 0. | 0. |
| C2 | 0.9584 | 0.9583 (0.9583) | 0. | 0. | 0. | 0. |
| C3 | 0.8334 | 0.8333 (0.8333) | 0.1666 | 0.1666 (0.1666) | 0.9997 | 0.9995 (0.9995) |
| C4 | 0.9165 | 0.9166 (0.9166) | 0.1665 | 0.1665 (0.1665) | 0.9999 | 0.9993 (0.9994) |
| C5 | 0.7916 | 0.7917 (0.7917) | 0.3332 | 0.3333 (0.3333) | 0.9999 | 0.9998 (0.9999) |
| C6 | 0.9584 | 0.9583 (0.9583) | 0.3331 | 0.3332 (0.3332) | 0.0006 | 0.0001 (0.0001) |
| C7 | 0.8333 | 0.8333 (0.8333) | 0.5 | 0.5 | 0. | 0. |
| C8 | 0.9165 | 0.9166 (0.9166) | 0.5 | 0.5 | 0. | 0. |
| $d_{c-c}$ | 1.434<d<1.449 | 1.426<d<1.428 (1.4256<d<1.4258) | | | | |

The space group is *Pccm*. The $\vec{c}$ axis is taken as perpendicular to the carbon planes. Using this convention, the $\vec{a}$, $\vec{b}$ and $\vec{c}$ axes correspond to the $\vec{c}$, $\vec{a}$ and $\vec{b}$ axes of the *Pccm* space group, respectively. The lattice parameters are in Å and the atomic positions in fractionary units of the crystal axes. The $d_g$ (along the $\vec{c}$ axis) interlayer distance is fixed at the experimental data. The distance between carbon atoms in a given carbon plane $d_{c-c}$ is in Å. The van der Waals corrected values are given in brackets

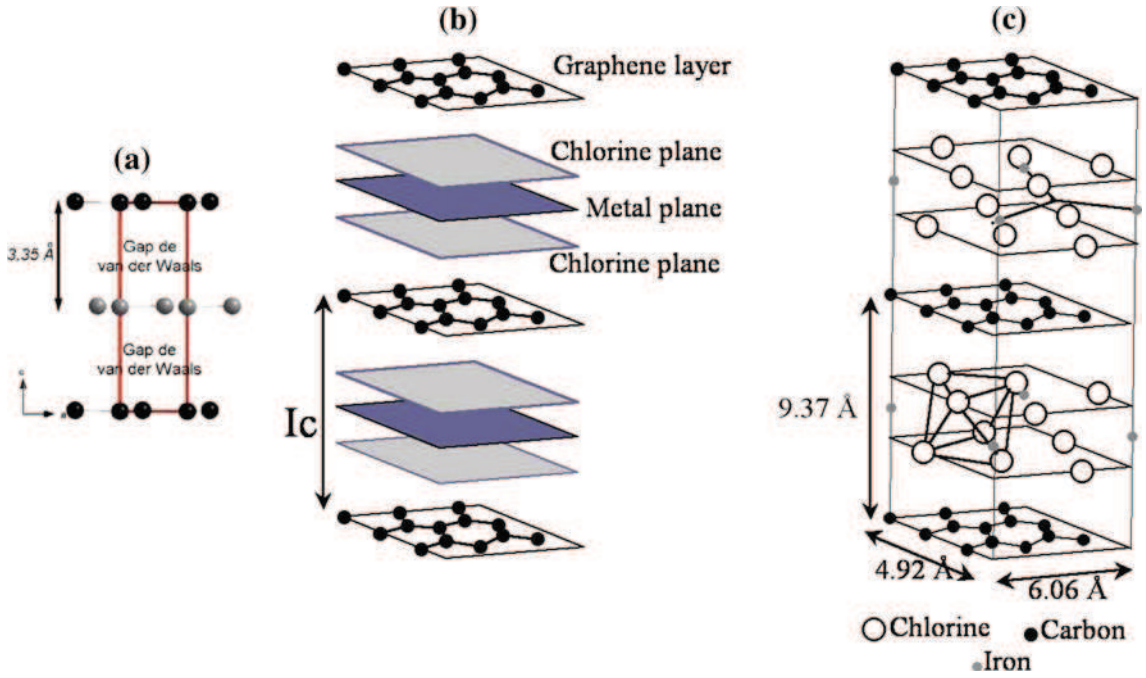


**Fig. 2** Schematic representation of the structure of graphite and $MCl_x$–GICs. In the case of graphite (**a**) the interlayer spacing is 3.35 Å. In the case of GICs (**b**) the van der Waals gap is occupied by intercalant molecules leading to an enhancement of the distance between graphene layers. The $FeCl_3$–GIC structure is presented in **c** [20]

case of $AlCl_3$–GIC. The ab initio band structure calculations are then carried out on this optimized structure.

In the case of the $FeCl_3$–GIC, the graphitic and the intercalant lattices are incommensurate [61], and the presence of $FeCl_3$ islands in the van der Waals gaps was pointed out by scanning tunnelling microscopy [62].

In the case of the $SbCl_5$–GIC, according to Mössbauer spectroscopy experiments, which point out the simultaneous presence of $Sb^{5+}$ ($SbCl_6^-$ and $SbCl_5$ species) and $Sb^{3+}$ ($SbCl_4^-$ and $SbCl_3$ species) ions in proportions depending on the synthesis conditions [31, 63], two intercalated species are present between the graphene sheets resulting from the chemical reaction [29]:

$$3SbCl_5 + 2e^- \Leftrightarrow 2SbCl_6^- + SbCl_3$$

In the case of the $AlCl_3$–GIC, the intercalated layers present two microstructures which coexist in the van der Waals gaps [28], depending on the synthesis conditions. The first one consists in disordered $Al_2Cl_6$ arrangements, while the second structure is characterized by ordered arrangements of $Al_2Cl_6$ molecules and $AlCl_4^-$ ions in an orthorhombic lattice commensurate with the graphite one [30, 64]. For ab initio calculations, the structure determination of $AlCl_3$–GIC was carried out using both experimental parameters deduced in the literature from X-ray diffraction ($\vec{c}$ axis, interlayer distance) and energy minimization process.

The optimized unit cell contains 64 atoms constituted of 48 carbon atoms in a flat hexagonal net, 4 aluminium atoms in the median plane of the cell and 12 chlorine atoms located between each carbon and aluminium planes. Therefore, the stoechiometry of the compound is $Al_4Cl_{12}C_{48}$ which is close to the experimental one, equal to $AlCl_{3.3}C_{9-10}$.

The resulting structure is presented in Fig. 3 and the corresponding parameters in Table 3. This cell is characterized by carbon planes in a weak corrugated hexagonal lattice. The distance between the carbon atoms along the graphene sheets is in the 1.43–1.45 Å range. Those results are in good agreement with the experimental data. The unit cell contains four $AlCl_3$ molecules where the Al atoms occupy the tetrahedral sites of a double layer of chlorine atoms. The corresponding Al–Cl distances are, respectively, 2.08 and 2.27 Å.

### 3.2 Electronic Structure of Pristine Graphite

The electronic structure of graphite was already studied in previous works [65–70]. The results obtained in this study allow us to validate the calculation approach and constitute the reference for the understanding of the electronic structure and interlayer interactions evolutions induced by intercalation.

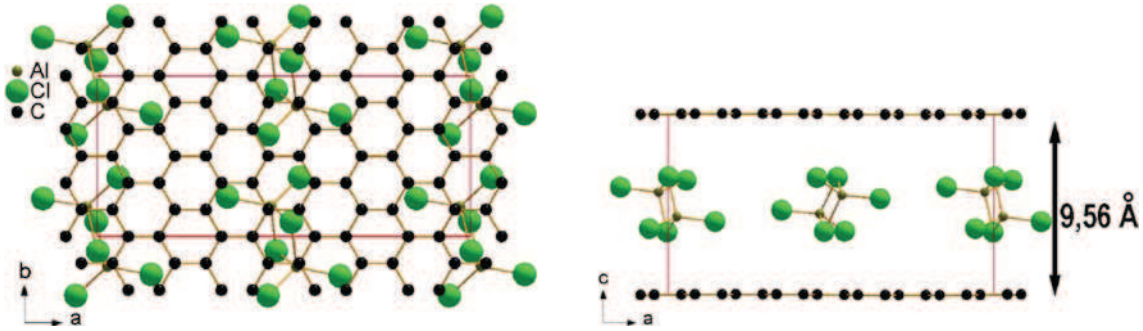


**Fig. 3** Crystal structure resulting from a geometrical optimization for $Al_4Cl_{12}C_{48}$

The bands structure and DOS diagrams of graphite are presented in Fig. 4a and b, respectively. The projected DOS on $\pi$ character points out that the top of the valence band and the bottom of the conduction one are constituted of $\pi$ and $\pi^*$ states, respectively. The DOS at Fermi level is very small [0.05 state/(eV cell)] but not zero conferring to graphite a semi-metal behaviour according to its electrical properties. The $\sigma$ and $\pi$ states are spread over a large range of energy ($-19$ eV to $-3$ eV for $\sigma$ and $-8$ eV to 0 eV for $\pi$) showing strong (covalent) interactions in the solid.

The First Brillouin Zone (FBZ) presented in Fig. 4c allows us to identify the paths, characterized by specific $k$-points at their extremities, along which the bands dispersions are studied and presented in bands diagrams. The K-Γ, Γ-M, H-A and A-L paths, for example, are parallel to $(\vec{a},\vec{b})$ planes and Γ-M, M-L and K-H are parallel to $\vec{c}$ axis. Bands energy dispersion along these paths will point out the strength of the orbital interactions along the corresponding directions. As large the bands dispersion are, as large the interaction strength along the considered directions are. Especially bands dispersion along Γ-M, M-L and K-H will characterize the intensity of interactions through the van der Waals gap.

The fat band diagrams presented in Fig. 4 emphasize by thick lines the $\sigma$ (d) and $\pi$ (e) contributions. $\sigma$ and $\pi$ bands strongly disperse along K-G-M-K and H-A-L-H paths parallel to $(\vec{a},\vec{b})$ planes according to the strong in-layer covalent interactions. However, $\pi$ bands slightly disperse along Γ-M, M-L and K-H paths (underlined by red rectangles) pointing out weak graphene interlayer interaction through the gap corresponding to slight $2p_z$ carbon orbital overlaps. The valence electron density map presented in Fig. 6 confirms these small overlaps through the gap by the presence of a slight electron density (0.04 e/Å$^3$) in the middle of the gap.

The estimated value of the interaction energy between layers, using the procedure described in Sect. 2.2, is of:

$$IE_G = -0.045 \text{ eV/at}$$

### 3.3 Electronic Structure of $AlCl_3$–GIC

Figure 5a–c presents the FBZ, the bands structure and the DOS diagrams corresponding to the $AlCl_3$–GIC optimized structure ($Al_4Cl_{12}C_{48}$ Fig. 3). As for graphite, the top of the valence band and the bottom of the conduction one are mainly $\pi$ and $\pi^*$ states, respectively. The Fermi level is slightly shifted in the $\pi$ states due to electron transfers from the graphene layers to electrophilic $AlCl_3$ intercalant, and the DOS at Fermi level is increased by comparison to graphite explaining the improvement by a 10 factor of the in-layer conductivity.

The bands structure diagram is rather complex with a great number of bands resulting of the size of the unit cell containing 64 atoms. Simultaneous examination of the DOS projected on the atomic characters and the bands structure diagram allows us to estimate the behaviour of the bands. The $\sigma$ (in red) and $\pi$ (in green) states are spread over energy ranges similar to those encountered in graphite. The corresponding bands strongly disperse over the S-Γ-X and S-R-Z-U paths parallel to the $(\vec{a},\vec{b})$ plane showing that the strong (covalent) in-layer carbon–carbon interactions are maintained. Along the X-S and R-U paths (underlined by red rectangles) orthogonal to $(\vec{a},\vec{b})$ planes, the bands do not reveal any significant dispersion. This strongly suggests that out of plane interactions are extremely weak (graphene–intercalant or graphene–graphene interactions) relatively to those encountered between graphene layers in graphite. This conclusion is strongly supported by the energy localisation of the aluminium and chlorine states, and the fact that their bands remain practically flat whatever the direction of the FBZ.

The valence electron density maps corresponding to the $AlCl_3$–GIC in graphene layer, perpendicular to graphene layers and in the middle of the van der Waals gap (parallel to $(\vec{a},\vec{b})$ plane) are presented in Fig. 6. The electron density distribution in the graphene layer seems not significantly affected by the intercalant molecules located in the van der Waals gap.

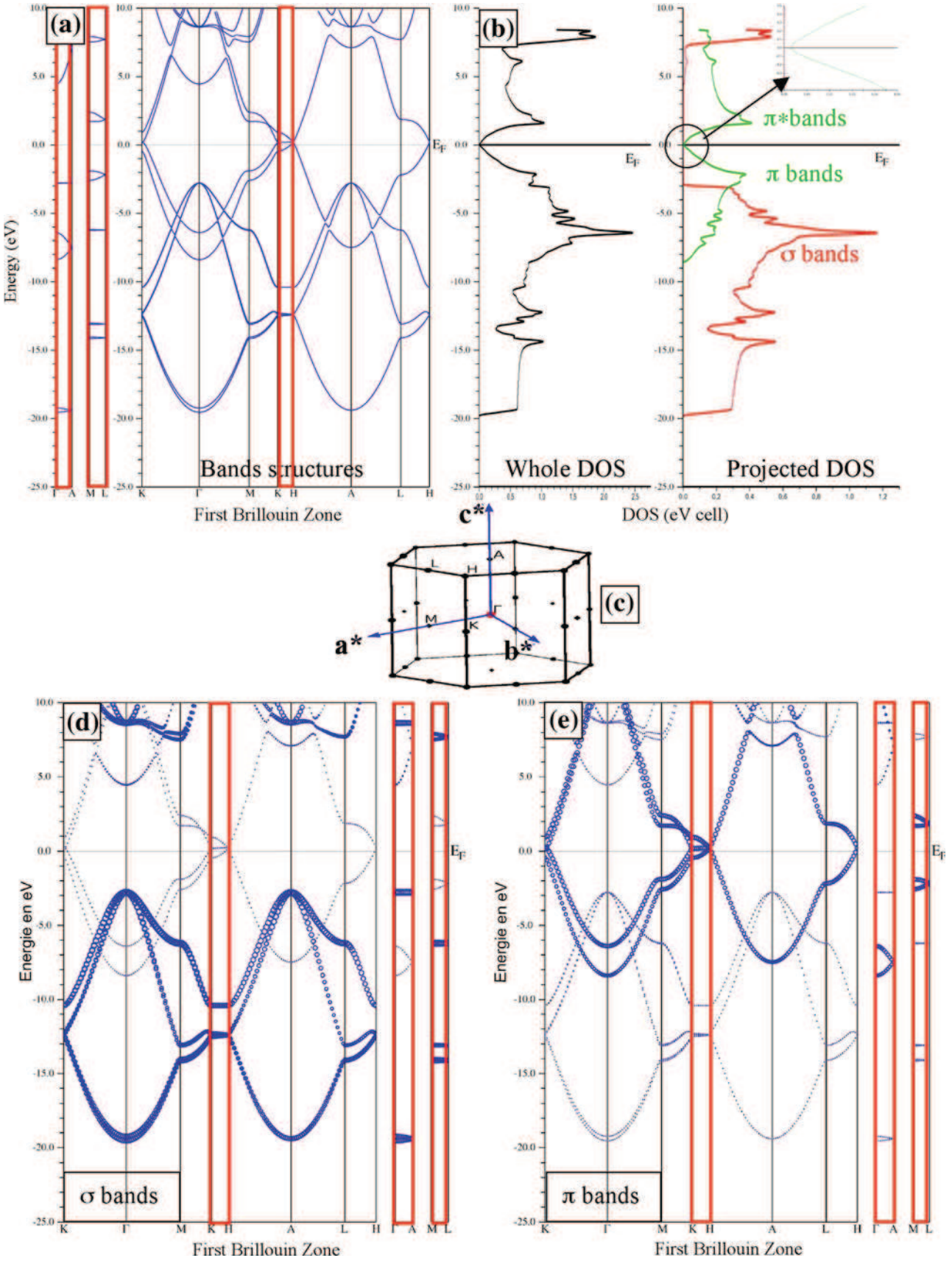
(a)
Energy (eV)
Bands structures
First Brillouin Zone
(b)
Whole DOS
Projected DOS
π*bands
π bands
σ bands
DOS (eV cell)
c*
a*
b*
(c)
(d)
σ bands
Energie en eV
First Brillouin Zone
(e)
π bands
Energie en eV
First Brillouin Zone

◀ **Fig. 4** **a** Bands structure diagrams. **b** whole and projected DOS for graphite. **c** First Brillouin Zone. **d**, **e** Fat bands diagrams emphasizing in thick lines the $\sigma$ and $\pi$ bands contributions. The superimposed *red* rectangles point out the directions parallel to $\vec{c}$ axis along which the bands dispersions are associated to orbitals overlaps through the van der Waals gap (Color figure online)

The calculated energy of the interaction between layers is estimated to graphite interlayer interaction in eV/at:

$$\mathrm{IE_{GIC}} = -0.001\ \mathrm{eV/at}$$

which is significantly lower than interlayer interactions in graphite.

As a conclusion, in $AlCl_3$–GIC, the bi-dimensional character is maintained. The interlayer interactions are reduced both by enhancement of the inter graphene layers distances and the very weak graphene–intercalant interactions emphasized by the band structure calculation results.

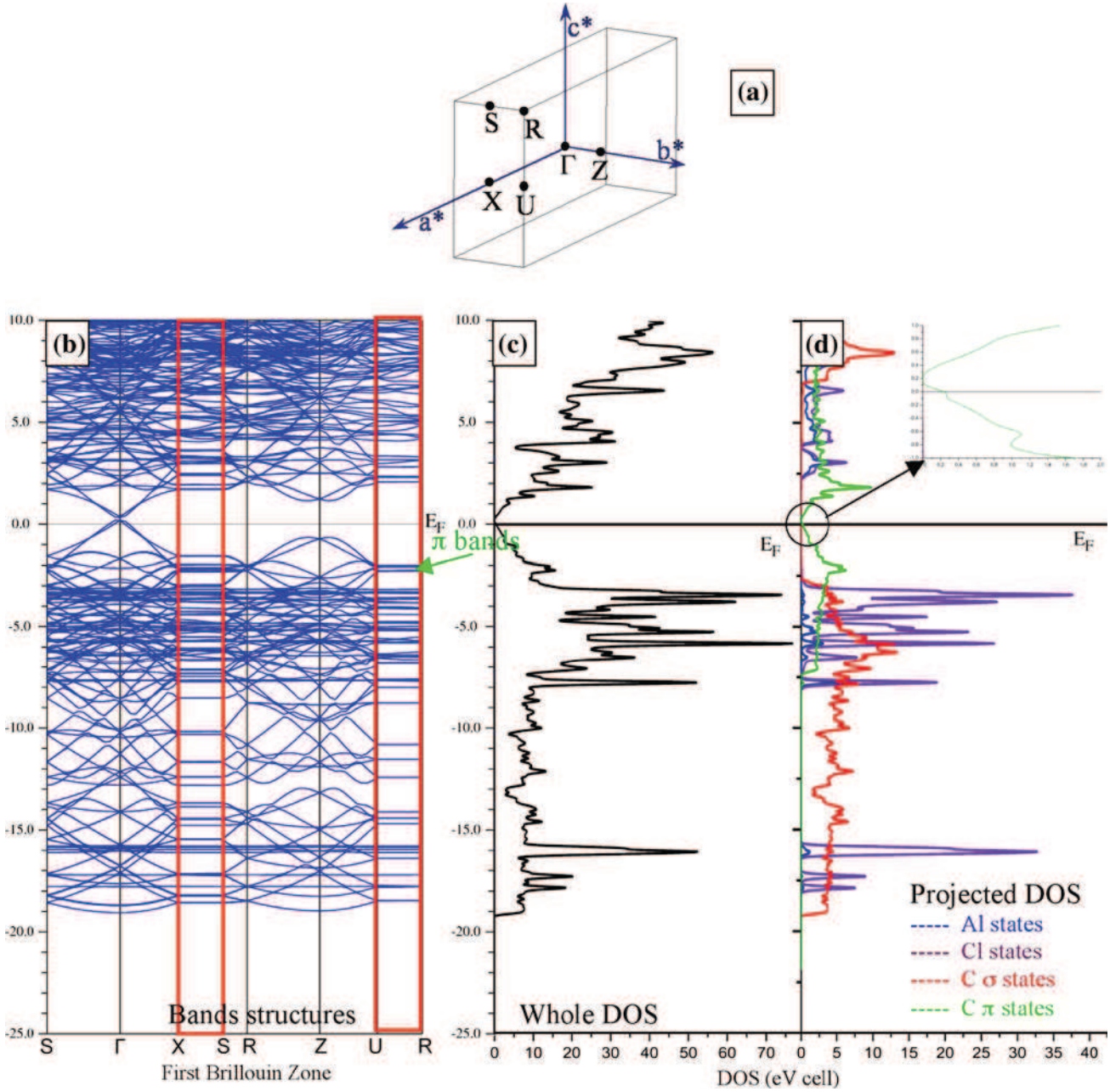


**Fig. 5** $AlCl_3$–GIC bands structure results. **a** First Brillouin Zone. **b** Bands structure diagram. **c**, **d** Whole and projected DOS. The absence of dispersion (flat bands) along the directions parallel to $\vec{c}$ axis (underlined by the *red* rectangles) strongly suggests the absence of overlap between intercalant and carbon orbitals inducing interlayer interactions weaker than in graphite (Color figure online)

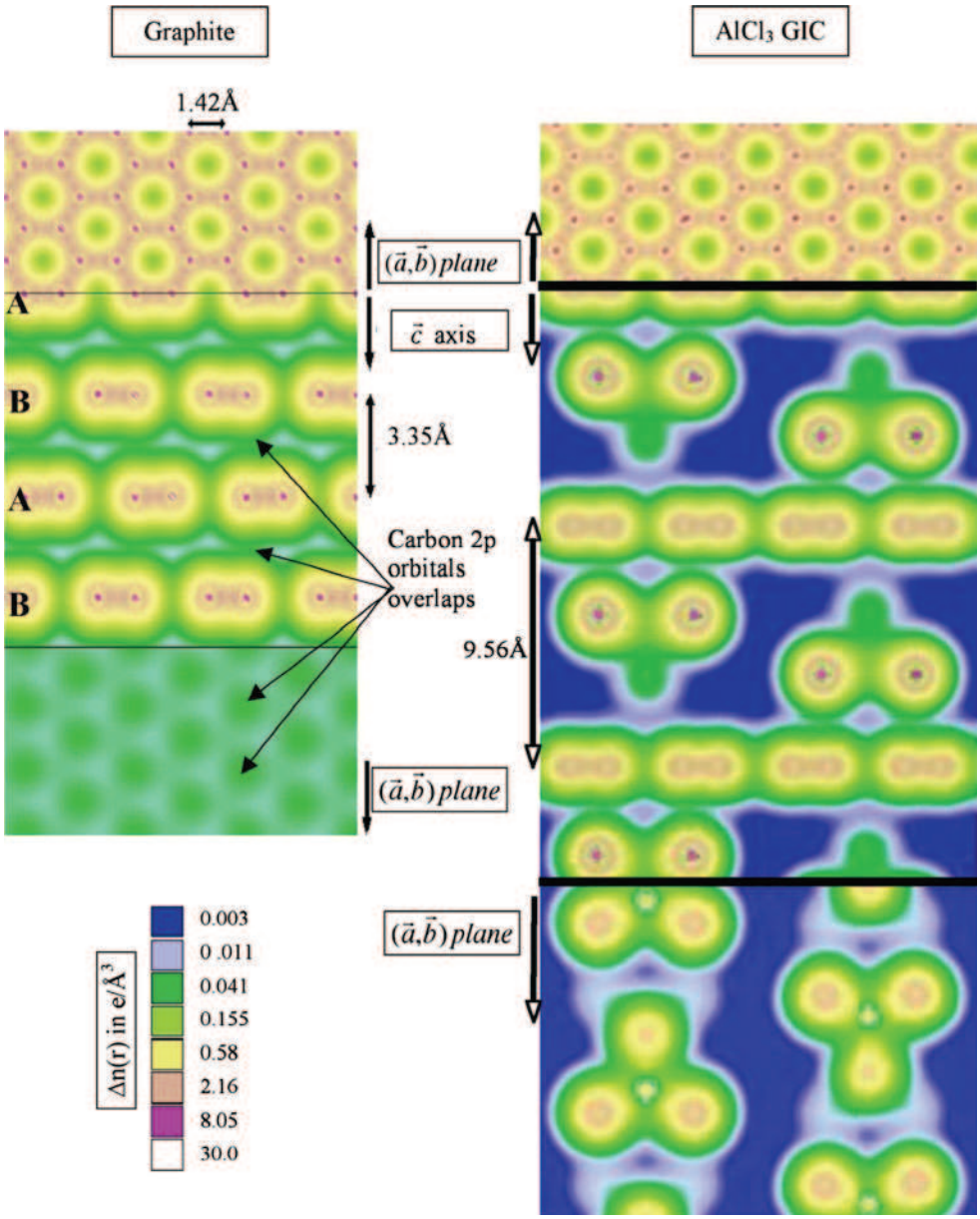


**Fig. 6** Valence electrons density maps in graphene layers, perpendicularly to graphene layers and in the middle of the van der Waals gap for graphite and the $AlCl_3$–GIC. In the case of graphite, a significant electron density between eclipsed carbon atoms (*arrows*) is clearly visible confirming the $2p_z$ carbon orbitals overlaps through the gap. The $AlCl_3$–GIC maps reveal weak electron density between graphene layer and chlorine atoms

Due to the strong similarities between the structures of the three studied GICs, the main conclusions obtained on $AlCl_3$–GIC are extended to the other ones.

### 3.4 Tribologic Properties

Due to the weak number of cycles used in order to study the intrinsic friction properties of the lamellar compounds, no significant wear was revealed during the tribologic experiments.

The friction coefficients recorded, under high-purity argon atmosphere, for pristine graphite and $FeCl_3$, $AlCl_3$ and $SbCl_5$–GICs are presented in Fig. 7. Whereas in the case of graphite, the friction coefficient presents an induction period before raising the steady friction coefficient of 0.22, the friction of all GICs starts at a value strongly inferior to the stabilized graphite friction coefficient. The friction coefficients obtained after three cycles, considered to correspond to the intrinsic friction properties of the compounds, are equal to 0.09 for the three GICs and confirm the possibility to use GICs as solid lubricants [71].

The friction behaviour recorded as a function of cycle number differs with the intercalated species. In the case of $FeCl_3$–GIC, a very good stability of the tribologic performances is noticed until the end of the friction. In the case of $AlCl_3$–GIC, the friction coefficient is stable over 60 cycles and progressively increases up to the value of graphite tribofilm. The $SbCl_5$–GIC exhibits the more unstable behaviour. The friction coefficient fluctuates between 0.09 up to 0.18 to finally stabilize at 0.15 after 60 cycles. The

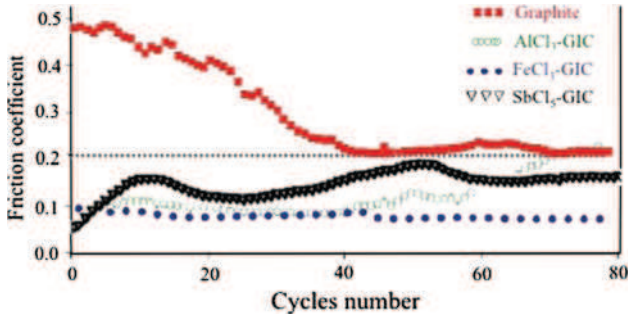


**Fig. 7** Friction coefficient evolution recorded under high-purity Ar atmosphere for the reference compound (graphite) and the three GICs

behaviour of the two last compounds strongly suggests evolutions of the structure and composition of these compounds during friction as de-intercalation process.

These conclusions are also supported by the tribologic results obtained in the presence of PE at the beginning of the friction tests. The results presented in Fig. 8 show the same behaviour for the three GICs. The friction coefficient in the presence of PE is of the order of 0.07 and raises a value of 0.09 just after PE evaporation. In the case of $FeCl_3$ and $AlCl_3$–GICs, the friction coefficients evolve by stabilized steps with rapid evolution between two steps which lets suppose a rapid evolution of the interfacial material such as de-intercalation.

In order to confirm this de-intercalation process, the initial $SbCl_5$–GIC and the corresponding tribofilms obtained after 10 and 80 cycles are investigated by means of Raman microspectrometry. Figure 9 presents the Raman spectra collected on (a) pristine graphite, (b) initial Stage 1 GIC before the friction test and (c, d) on tribofilms.

The Raman spectrum of pristine graphite (Fig. 9a) exhibits one large band at 1,580 $cm^{-1}$ assigned to optical $E_{2g}$ vibration mode of the carbon atoms (G band) and two small peaks at 1,350 and 1,620 $cm^{-1}$, respectively, attributed to disorder (D and D' bands) [20, 72, 73].

The initial $SbCl_5$–GIC (Fig. 9b) presents only one peak at 1,627 $cm^{-1}$ in its Raman spectrum. This peak corresponds to the G band. The energy shift, compared to graphite, is associated to the electron transfers from the graphene layers to the intercalant molecules.

The Raman spectrum recorded on the tribofilm obtained after 10 cycles (Fig. 9c) exhibits one main band at 1,610 $cm^{-1}$ corresponding to an intercalation stage superior to 1 [72] and three small peaks at 1,627 $cm^{-1}$ (Stage 1 $SbCl_5$–GIC), 1,580 and 1,350 $cm^{-1}$ (G and D bands of graphite). The presence of de-intercalated GIC in the tribofilm obtained after 10 cycles points out that a de-intercalation process occurs in the early instant of friction. The Raman analysis of the tribofilm obtained after 80 cycles (Fig. 9d) only exhibits the D and G bands of

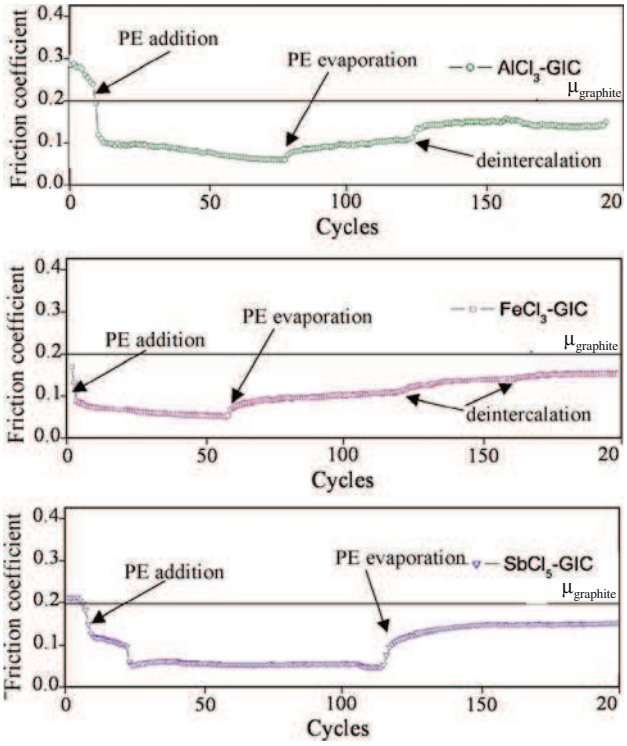


**Fig. 8** Friction coefficient evolution for the three GICs obtained when one drop of PE is added at the beginning of the test in order to facilitate the tribofilm formation. The friction properties of the various compounds are measured after the evaporation of the PE. As it is clearly seen for $AlCl_3$ and $FeCl_3$–GICs, the friction coefficient evolves by step pointing out structural and chemical evolutions of the GICs (de-intercalation phenomena) in the tribologic interface during friction leading to a deterioration of their tribologic properties

graphite. The high value of the D/G intensity ratio compared to graphite demonstrates the highly disordered character of the tribofilm structure.

Raman spectroscopy clearly shows that in the case of $SbCl_5$–GIC, the de-intercalation phenomenon is complete after 80 cycles which can explain the obtained friction coefficient close to 0.2.

## 4 Discussion

The intrinsic tribologic properties of metal chloride $MCl_x$ GICs clearly demonstrate that the intercalation of species in the van der Waals gaps strongly influences the friction behaviour of initial graphite.

The correlation of the tribologic data to the electronic studies shows that the intercalation of $MCl_x$ species into graphite strongly improves the friction performances ($0.07 < \mu < 0.09$ compared to 0.2 for pure graphite). This beneficial effect is attributed to the large enhancement of the van der Waals gaps and the weak interactions between the intercalant and the graphene layers leading to the easy

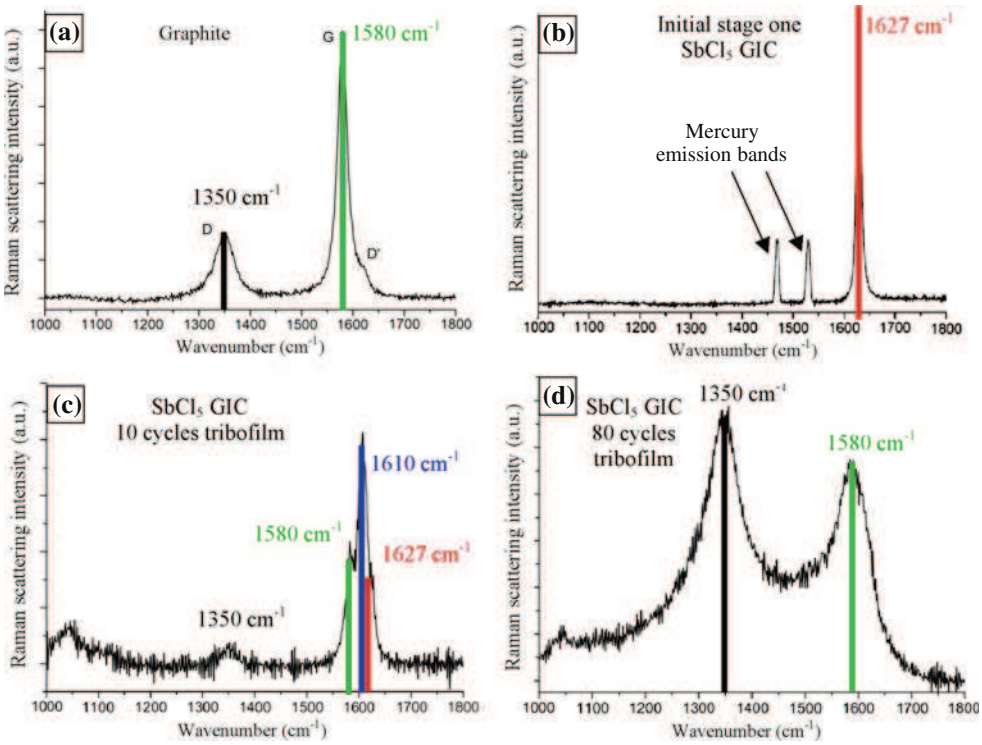


**Fig. 9** Raman spectra recorded on **a** pristine graphite; **b** initial stage-1 $SbCl_5$–GIC before the friction test; **c** tribofilm after 10 cycles and **d** tribofilm at the end of the tribologic test. The *two lines* present at 1,464 $cm^{-1}$ and 1,527 $cm^{-1}$ in the spectrum **b** are the emission lines of a vapour mercury lamp used as internal standards. As it is clearly demonstrated, de-intercalation process occurs during friction leading at the end of the test to tribofilm mainly composed of ill organized carbon

cleavage along direction parallel to $(\vec{a}, \vec{b})$ planes (due to the weakening of interlayer interactions through the van der Waals gap).

Evolution of the friction coefficient as a function of cycle numbers shows that the durability of the performances depends on the nature of the intercalated species. If a good stability is obtained in the case of $FeCl_3$–GIC, de-intercalation occurs during friction test leading to a deterioration of friction properties for $AlCl_3$ and $SbCl_5$–GICs. This interpretation is strongly supported by Raman analyses which points out that de-intercalation is partially achieved after 10 cycles and complete after 80 cycles in the case of the $SbCl_5$–GIC.

## 5 Conclusion

Tribologic experiments carried out on pristine graphite and transition metal chloride GICs demonstrate that intercalation of electrophilic species in the van der Waals gap modifies tribologic behaviour.

Due to ill-organized distribution of intercalant species in the van der Waals gap of graphite, bands structures and energy calculations were carried out for the $AlCl_3$–GIC on an optimized structure based on experimental deduced parameters ($\vec{c}$ axis, interlayer distance) and energy minimization. The main results show an interlayer interaction lower for the intercalated compounds than for graphite which is considered to be at the origin of the friction properties improvement of graphite by the intercalation process.

Evolution of the GIC friction properties during friction test associated to Raman analyses of the tribofilm at different steps of the experiments demonstrate that in the case of steel surfaces, de-intercalation process occurs in the case of $AlCl_3$ and $SbCl_5$–GICs, leading to a degradation of the friction performances of the built tribofilm.

As a conclusion, intercalation of electrophilic species in the van der Waals gap of graphite leads to friction properties improvement mainly attributed to the weakening of interlayer interaction resulting in easy shearing along direction parallel to $(\vec{a}, \vec{b})$ planes.

**Acknowledgments** The authors wish to thank the $C^3I$ for its technical support in collecting computational data. The authors acknowledge the French Research Department, the Conseil Régional de la Guadeloupe, the Fond Social Européen (FSE) and the Fond Européen pour le Développement (FEDER) for their financial supports.

## References

1. Takur, D.S., Delmon, B.: The role of group VIII metal promoter in $MoS_2$ and $WS_2$ hydrotreating catalysts: I. ESR studies of Co-Mo, Ni-Mo and Ni-W catalysts. J. Catal. **91**, 308–317 (1985)

2. Vazquez, A.: High resolution electron microscopy of $MoS_2$:Ni, $MoS_2$:Co and $MoS_2$:Fe layered crystals. Mater. Lett. **35**, 22–27 (1998)
3. Benavente, E., Santa Ana, M.A., Mendizabal, F., Gonzalez, G.: Intercalation chemistry of molybdenum disulfide. Coord. Chem. Rev. **224**, 87–109 (2002)
4. Yen, B.K.: Influence of water and oxygen on the tribology of carbon materials with $sp^2$ valence configuration. Wear **192**, 208–215 (1996)
5. Williams, J.A., Morris, J.H., Ball, A.: The effect of transfer layers on the surface contact and wear of carbon-graphite materials. Tribol. Int. **30**, 663–676 (1997)
6. Grill, A.: Diamond-like carbon: state of the art. Diamond Rel. Mater. **8**, 428–434 (1999)
7. Teer, D.G.: New solid lubricant coatings. Wear **251**, 1068–1074 (2001)
8. Moore, S.E., Lunsford, J.H.: The role of hydrogen in the reaction of water with surface carbon to form methane. J. Catal. **77**, 297–300 (1982)
9. Ubbelohde, A.R.: Electronic properties of some synthetic metals derived from graphite. Proc. R. Soc. A **327**, 289–303 (1972)
10. Weinberger, B.R., Kaufer, J., Heeger, A.J., Falardeau, E.R., Fischer, J.E.: Nuclear magnetic resonance and static magnetic susceptibility of $AsF_5$-intercalated graphite. Solid State Commun. **27**, 163–167 (1978)
11. Vogel, F.L., Fuzellier, H., Zeller, C., McRae, E.J.: In-plane electrical resistivity of nitric acid intercalated graphite. Carbon **17**, 255–257 (1979)
12. Batallan, F., Rosenman, I., Simon, C., Furdin, G., Fuzellier, H.: The electronic structure of the graphite acceptor compounds. Physica B + C **99**, 411–414 (1980)
13. Elzinga, M., Morelli, D.T., Uher, C.: Thermal transport properties of $SbCl_5$ graphite. Phys. Rev. B **26**, 3312–3319 (1982)
14. Issi, J.P., Heremans, J., Dresselhaus, M.S.: Electronic and lattice contributions to the thermal conductivity of graphite intercalation compounds. Phys. Rev. B **27**, 1333–1347 (1983)
15. El-Shazly, O.: In plane and c-axis transport properties of $FeCl_3$–GIC. Synth. Met. **83**, 81–84 (1996)
16. Dresselhaus, M.S.: Intercalation in Layered Materials. Plenum Press, New York (1986)
17. Kirczenow, G.: Staging and kinetics. In: Zabel, H., Solin, S.A. (eds.) Graphite Intercalation Compounds I—Structure and Dynamics, pp. 59–100. Springer, Berlin
18. Enoki, T., Endo, M., Suzuki, M.: In: Graphite Intercalation Compounds and Applications. Oxford University Press, New York (2003)
19. Fredenhagen, K., Cadenbach, G.: Die Bindung von Kalium durch Kohlenstoff. Z. Anorg. Allgem. Chem. **158**, 249–263 (1926)
20. Dresselhaus, M.S., Dresselhaus, G.: Intercalation compounds of graphite. Adv. Phys. **51**, 1–186 (2002)
21. Bagouin, M., Guérard, D., Hérold, A.: Action de la vapeur de lithium sur le graphite. CR Acad. Sci. Paris **C262**, 557–559 (1966)
22. Guérard, D., Hérold, A.: Nouvelles méthodes de préparation des composés d'insertion du lithium. CR Acad. Sci. Paris **C275**, 571–573 (1972)
23. Guérard, D., Hérold, A.: Intercalation of lithium into graphite and other carbons. Carbon **13**, 337–345 (1975)
24. Yazami, R, Cherigui, A., Nalimova, V.A., Guérard, D.: The carbon–lithium electrodes for secondary batteries. In: Proceedings of the 2nd Meeting of Electrochemical Society, Toronto (1992)
25. Fong, R., von Sacken, U., Dahn, J.R.: Studies of lithium intercalation into carbons using nonaqueous electrochemical cells. J. Electrochem. Soc. **137**, 2009–2013 (1990)
26. Billaud, D., Henry, F.X., Willmann, P.: Electrochemical synthesis of binary graphite–lithium intercalation compounds. Mater. Res. Bull. **28**, 477–483 (1993)
27. Pietronero, L., Strässler, S., Zeller, H.R., Rice, M.J.: Charge distribution in lamellar graphite acceptor intercalation compounds. Phys. Rev. Lett. **41**, 763–767 (1978)
28. Vangelisti, R., Lelaurain, M., Batallan, F.: Phase et transformation de phase dans les composés graphite-$AlCl_3$ de $1^{er}$ stade. Carbon **24**, 654–656 (1986)
29. Homma, H., Clarke, R.: Structural phase transitions in $SbCl_5$-intercalated graphite. Phys. Rev. B **31**, 5865–5877 (1985)
30. Behrens, P., Wiegand, U., Metz, W.: In-plane structure of the aluminium chloride intercalated in graphite. Carbon **86**, 502–504 (1986)
31. Wortmann, G., Godler, F., Perscheid, B., Kaindl, G., Schlögl, R.: Chemical and microstructural organization of graphite intercalated with $SbCl_5$ and $SbF_5$ from $^{121}$Sb-Mössbauer spectroscopy. Synth. Met. **26**, 109–137 (1988)
32. Walter, J., Shioyama, H., Sawada, Y., Harab, S.: Electron diffraction and scanning tunneling microscope studies of $TaCl_5$-graphite intercalation compounds. Carbon **36**, 1277–1284 (1998)
33. Find, J., Herein, D., Uchida, Y., Schlögl, R.: A new three-dimensional structural model for the $CuCl_2$ graphite intercalation compound. Carbon **37**, 1431–1441 (1999)
34. Walter, J., Shioyama, H.: Boron trichloride graphite intercalation compound studied by selected area electron diffraction and scanning tunneling microscopy. J. Phys. Chem. Solids **60**, 737–741 (1999)
35. Rüdorff, W., Schulz, H.: The intercalation of iron(II) chloride in the crystal lattice of graphite. Anorg. Allg. Chem. **245**, 121–156 (1940)
36. Rüdorff, W., Zeller, R.: Aluminium chloride graphite intercalation compounds. Zeit. Anorg. Allg. Chem. **279**, 182–193 (1955)
37. Dailly, A., Ghanbaja, J., Willmann, P., Billaud, D.: Electrochemical intercalation of lithium into graphite-antimony composites synthesized by reduction of a SbCl5–graphite intercalation compound by gaseous caesium. J. Power Sources **125**, 70–76 (2004)
38. Thomas, P., Himmel, D., Mansot, J.L., Dubois, M., Guérin, K., Zhang, W., Hamwi, A.: Tribological properties of fluorinated carbon nanofibres. Tribol. Lett. **34**, 49–59 (2009)
39. Thomas, P., Himmel, D., Mansot, J.L., Zhang, W., Dubois, M., Guérin, K., Hamwi, A.: Friction properties of fluorinated carbon nanodiscs and nanocones. Tribol. Lett. **41**, 353–362 (2011)
40. Blaha, P., Schwarz, K., Madsen, G., Kvasnicka, D., luitz, J.: WIEN2k, An Augmented Plane Wave + Local Orbitals Program for Calculating Crystal Properties. Technische Universität Wien, Austria (2001)
41. Dovesi, R., Orlando, R., Civalleri, B., Roetti, C., Saunders, V.R., Zicovich-Wilson, C.M.: CRYSTAL: a computational tool for the ab initio study of the electronic properties of crystals. Z. Kristallogr. **220**, 571–573 (2005)
42. Dovesi, R., Saunders, V.R., Roetti, C., Orlando, R., Zicovich-Wilson, C.M., Pascale, F., Civalleri, B., Doll, K., Harrison, N.M., Bush, I.J., D'Arco, P., Llunell, M.: CRYSTAL09 User's Manual. University of Torino, Torino (2009)
43. Kresse, G., Hafner, J.: Ab initio molecular-dynamics simulation of the liquid-metal-amorphous-semiconductor transition in germanium. Phys. Rev. B **49**, 1425–14269 (1994)
44. Kresse, G., Furthmüller, J.: Efficiency of ab initio total energy calculations for metals and semiconductors using a plane-wave basis set. Comput. Mater. Sci. **6**, 15–50 (1996)
45. Kresse, G., Furthmüller, J.: Efficient iterative schemes for ab initio total-energy calculations using a plane-wave basis set. Phys. Rev. B **54**, 11169–11186 (1996)
46. Paier, J., Hirsch, R., Marasman, M., Kresse, G.: The Perdew-Burke-Ernzerhof exchange-correlation functional applied to the G2-1 test set using a plane-wave basis set. J. Chem. Phys. **122**, 234102–234114 (2005)

47. Franchini, G., Bayer, V., Podloucky, R., Paier, J., Kresse, G.: Density functional theory study of MnO by an hybrid functional approach. Phys. Rev. B **72**, 045132–045136 (2005)
48. Vanderbilt, D.: Soft self-consistent pseudopotentials in a generalized eigenvalue formalism. Phys. Rev. B **41**, 7892–7895 (1990)
49. Kresse, G., Joubert, D.: From ultrasoft pseudopotentials to the projector augmented-wave method. Phys. Rev. B **59**, 1758–1775 (1999)
50. Blöchl, P.E.: Projector augmented-wave method. Phys. Rev. B **50**, 17953–17979 (1994)
51. Perdew, J.P., Chevary, J.A., Vosko, S.H., Jackson, A., Pederson, M.R., Singh, D.J., Fiolhais, C.: Atoms, molecules, solids, and surfaces: applications of the generalized gradient approximation for exchange and correlation. Phys. Rev. B **46**, 671–687 (1992)
52. Monkhorst, H.J., Pack, J.D.: Special points for Brillouin-zone integrations. Phys. Rev. B **13**, 188–192 (1976)
53. Grimme, S.: Accurate description of van der Waals complexes by density functional theory including empirical corrections. J. Comput. Chem. **25**, 1463–1473 (2004)
54. Grimme, S.: Semi empirical GGA-type density functional constructed with a long-range dispersion correction. J. Comput. Chem. **27**, 1787–1799 (2006)
55. Labat, F., Baranek, P.H., Domain, C., Minot, C., Adamo, C.: Density Functional analysis of the structural and electronic properties of $TiO_2$ rutile and anatase polytypes : performances of different exchange-correlation functionals. J. Chem. Phys. **126**, 154703–154712 (2007)
56. Hermansson, K., Probst, M.M., Gajewski, G., Milev, P.D.: An harmonic OH vibrations in $Mg(OH)_2$ (Brussite): two dimensional calculation and crystal induced blue shift. J. Chem. Phys. **131**, 244517–244528 (2009)
57. Civalleri, B., Zicovich-Wilson, C.M., Valenzano, L., Ugliengo, P.: B3LYP augmented with an empirical dispersion term (B3LYP-D*) as applied to molecular crystals. Cryst. Eng. Commun. **10**, 405–410 (2008)
58. Ugliengo, P., Zicovich-Wilson, C.M., Tosoni, S., Civalleri, B.: Role dispersive interactions in layered materials: a periodic B3LYP and B3LYP-D* study of $Mg(OH)_2$, $CaOH)_2$ and kaolinite. Mater. Chem. **19**, 2564–2572 (2009)
59. Bucko, T., Hafner, J., Lebègue, S., Angyan, J.G.: Improved description of the structure of molecular and layered crystals: ab initio DFT calculations with van der Waals corrections. J. Phys. Chem. A **114**, 11814–11824 (2010)
60. Boca, M.H., Saylors, M.L., Smith, D.S., Eklund, P.C.: X-ray study of the layer structure of graphite-antimony chloride intercalation compounds. Synth. Met. **6**, 39–51 (1983)
61. Cowley, J.A.: The structure of some ferric chloride-graphite compounds. Acta Crystallogr. A **9**, 421–431 (1956)
62. Gauthier, S., Rousset, S., Klein, J., Sacks, W., Belin, M.: A study of graphite and intercalated graphite by scanning tunneling microscopy. J. Vac. Sci. Technol. A **6**, 360–362 (1988)
63. Boolchand, P., Bresser, W.J., McDaniel, D., Sisson, K., Yeh, V., Eklund, P.C.: Identification of the intercalant species in SbCl5-graphite using Mössbauer spectroscopy. Solid State Commun. **40**, 1049–1053 (1981)
64. Nagai, K., Kurata, H., Isoda, S., Kobayashi, T.: Three-dimensional structure of $AlCl_3$ in stage-1 $AlCl_3$–GIC. Synth. Met. **45**, 27–34 (1992)
65. Wallace, P.R.: The band theory of graphite. Phys. Rev. **71**, 622–634 (1947)
66. Slonczewski, J.C., Weiss, P.R.: Band structure of graphite. Phys. Rev. **109**, 272–279 (1958)
67. McLure, J.W.: Band structure of graphite and de Hass-van Alphen effect. Phys. Rev. **108**, 409–410 (1958)
68. Zunger, A.: Self-consistent LCAO calculation of the electronic properties of graphite. I. The regular graphite lattice. Phys. Rev. B **17**, 626–641 (1978)
69. Holzwarth, N.A.W., Louie, S.G., Rabii, S.: X-ray form factor and the electronic structure of graphite. Phys. Rev. B **26**, 5382–5390 (1982)
70. Charlier, J.C., Gonze, X., Michenaud, J.: First-principle study of the electronic properties of graphite. Phys. Rev. B **43**, 4579–4589 (1991)
71. Conte, A.A.: Graphite intercalation compounds as solid lubricants. ASLE Trans. **26**, 200–208 (1983)
72. Dresselhaus, M.S., Pimenta, M.A., Ecklund; P.C., Dresselhaus, G.: Raman scattering in fullerenes and related carbon-based materials. In: Weber, W.H., Merlin, R. (eds.), pp. 315–364. Springer, New York (2000)
73. Merlin, R., Pinczuk, A., Weber, W.H.: Overview of phonon. Raman scattering in solids. In: Weber, W.H., Merlin, R. (eds.) Raman Scattering in Material Science, pp. 1–29. Springer, New York (2000)